Korean J. Chem. Eng., 40(10), 2529-2537 (2023)
DOI: 10.1007/s11814-023-1428-9

pISSN: 0256-1115
eISSN: 1975-7220

Facile synthesis of polynorbornene-based binder through ROMP for silicon anode in lithium-ion batteries

Anjali Nagapadi Preman*, Ye Eun Lim, Seungjae Lee*, Seokjun Kim***, Il Tae Kim**,†, and Suk-kyun Ahn*,†**

*School of Chemical Engineering, Pusan National University, Busan 46241, Korea
**Department of Chemical and Biological Engineering, Gachon University, Seongnam-si, Gyeonggi-do 13120, Korea
***School of Mechanical Engineering, Pusan National University, Busan 46241, Korea
(*Received 28 January 2023 • Revised 10 February 2023 • Accepted 13 February 2023*)

Abstract−Although binders are a minor component in battery electrodes, they can improve the electrochemical performance considerably, particularly in conversion-type electrodes, such as the silicon (Si) anode, which has volume expansion problems. Although numerous binders are reported for Si anode, less attention has been paid to those prepared through controlled polymerization, which can allow the preparation of well-defined polymers. Herein, we report the facile synthesis of carboxylic acid-functionalized polynorbornene (CA-PNB) via ring-opening metathesis polymerization (ROMP) and apply this as the binder for Si anode. Owing to the ultrafast polymerization kinetics of ROMP, a high molecular weight polymer (~279 kDa) with narrow dispersity (Đ=1.07) was readily prepared within 30 min. The resulting CA-PNB was used as the binder for a Si nanoparticle anode, which exhibits an initial coulombic efficiency of 81% and a specific capacity of 1,654 mAh g^{-1} after 100 cycles at 0.5 A g^{-1}. These values outperform the Si anodes prepared using conventional polyvinylidene difluoride and carboxymethyl cellulose binders, probably due to the abundant carboxylic acid groups in the CA-PNB that offer stronger interactions with the Si surface. Since ROMP is a highly efficient polymerization tool to produce polymers with tailored architectures and controlled monomer sequences, this method will be valuable for the rational molecular design of high-performance binders for battery electrodes.

Keywords: Silicon Anodes, Polymer Binders, ROMP, Lithium-ion Batteries, Polynorbornene

INTRODUCTION

The development of lithium-ion batteries (LIBs) with high energy density is essential for meeting the rapidly growing demand for sustainable energy. Silicon (Si) has been studied extensively as one of the most promising anode materials in the past decade [1-3]. Si has a high theoretical specific capacity (3,570 mAh g^{-1} when alloyed into $Li_{4.4}Si$), which is nearly ten times greater in magnitude than conventional graphite anodes [4]. In addition, its low operation potential (~0.4 V vs. Li/Li^+), earth abundance, and mature processing techniques are also attractive for commercialization. However, the drastic volume changes (up to 300%) of Si during the lithiation-delithiation process cause considerable internal stress, leading to structural damage to the electrode and capacity decay. Various structural modifications have been suggested to solve these problems, including porous Si [5,6], nano Si [7,8], core-shell Si [9], and Si-carbon composites [10,11]. However, the high cost and complex process synthesis limit their large-scale production for commercial batteries.

The development of robust binders can be an alternative strategy to deal with the volume changes and related problems of the Si anode and is possibly more cost-effective than structural modification of Si. Despite the small content in the electrode (typically <20 wt%), binders are essential for providing mechanical and conductive integrity because the major function of binders is to tightly hold active materials and conductive additives to the current collector during battery operation [12]. The choice of binder is also critical for adequate mixing and uniform dispersion of active/conductive materials in the slurry to prepare a homogeneous electrode. In addition, the binders also help to form a stable solid electrolyte interphase (SEI) layer on the Si surface to prevent overreactions between Si and the electrolyte [13,14]. Considering the numerous silanol groups (Si-OH) on the surface of Si particles, binders that can form strong bonds through covalent or non-covalent interactions with silanol groups are strongly encouraged. In this regard, natural or synthetic polymers comprising polar functional groups, such as -OH, -COOH, or $-NH_2$, have been extensively explored [15-19]. Representative examples of such binders include poly(acrylic acid) [12,20-23], poly(vinyl alcohol) [24,25], polyacrylamide [26-28], and polysaccharide [29-34].

While numerous functional binders for silicon anodes have been reported, the use of controlled polymerization techniques has been less explored [35-38], possibly due to the low cost-efficiency. Nevertheless, controlled polymerization methods have great potential to prepare well-defined polymers, such as tailored polymer architectures (graft, star, bottlebrushes, and cyclic structures) and controlled monomer sequences (block, random, alternating, and gradient) along with narrow molecular weight distribution [39-41]. These features can offer an additional molecular-design capability to produce useful binders for battery electrodes, and they are worth

†To whom correspondence should be addressed.
E-mail: itkim@gachon.ac.kr, skahn@pusan.ac.kr

more investigation in the future.

In this study, we exploited ring-opening metathesis polymerization (ROMP), a renown controlled polymerization technique, to synthesize binders for silicon anodes. As a model binder, carboxylic acid-functionalized polynorbornene (CA-PNB) was synthesized using a two-step process including the ROMP of t-butyl ester-functionalized norbornene, followed by deprotection of the t-butyl moiety, generating carboxylic acid groups. In particular, high molecular weight polymer (279 kDa) with narrow molecular weight distribution (Đ=1.07) can be synthesized within 30 min owing to the ultrafast polymerization kinetics of ROMP. Obtaining a large molecular weight polymer (>100 kDa) within a short period in a controlled manner is an attractive feature because the molecular weight has a great influence on the ultimate performance of the binders in the electrode [42]. To the best of our knowledge, CA-PNB was first employed as a binder in Si nanoparticle anodes. Interestingly, the Si anodes prepared using CA-PNB binders outperformed Si anodes prepared using polyvinylidene difluoride (PVDF) and carboxymethyl cellulose (CMC) binders in electrochemical performance (specific capacity and cycling stability). The superior performance of CA-PNB binders was attributed to the abundant -COOH groups and the long polymer chain that ensures strong interaction with the Si surface.

EXPERIMENTAL

1. Materials

Tert-butyl 5-norbornene-2-carboxylate (NB*t*BC, mixture of *endo* and *exo*, 95%) was purchased from Tokyo Chemical Industry. Trifluoroacetic acid (TFA, 99%), dimethyl sulfoxide (DMSO), and N-methyl-2-pyrrolidone (99.5%) were purchased from Sigma-Aldrich. Dichloromethane (DCM, stabilized with ethanol, 99+%) and ethyl vinyl ether (EVE, 99%) were obtained from Acros Organics. Nano-Si powder (APS ≤50 nm, 98%) and Super P (99+%) were supplied by Alfa Aesar. All reagents and solvents were used without further purification. $(H_2IMes)(pyr)_2(Cl)_2RuCHPh$ (third generation Grubbs catalyst, G3) was prepared according to a reported protocol [43] and used immediately. CMC (M_w ~150 kDa) was procured from Daicel Miraizu Ltd., and PVDF (M_w ~534 kDa) was acquired from Sigma-Aldrich.

2. Synthesis of Carboxylic Acid-functionalized Polynorbornene Binder (CA-PNB)

NB*t*BC (3 g, 15.442 mmol) was placed in an oven-dried round bottom flask equipped with a magnetic stir bar, capped with a rubber septum, and purged with nitrogen. Dry DCM (64 mL) was introduced to this flask to dissolve the NB*t*BC monomer. A G3 solution (7 mg mL^{-1}, 0.01 mmol) in DCM was prepared separately in an oven-dried scintillation vial, capped with a rubber septum, and purged with nitrogen. Polymerization was started by transferring the catalyst solution to the NBtBC solution using the cannula method and stirring for 30 min at room temperature. Polymerization was terminated by adding 1 mL of EVE to the reacting solution and stirring for an additional 10 min. Subsequently, the solvent was removed using a rotary evaporator, and the crude polymer was purified by repeatedly precipitating into excess methanol and drying for 24 h in a vacuum oven at room temperature.

The t-butyl-protecting group of the synthesized polymer was cleaved by a TFA treatment. The dried polymer (2 g) was re-dissolved in DCM (14 mL), and TFA (3.15 mL, 41.2 mmol) was added to the polymer solution under nitrogen. The resulting mixture was then stirred for 18 h at room temperature. The reaction mixture was subjected to rotary evaporation to remove the solvent and residual TFA. The final product was obtained after purification by precipitating into excess hexane and dried for 24 h in a vacuum oven at room temperature.

3. Characterization

^{1}H NMR spectra were recorded on a Varian Unity Inova spectrometer (500 MHz) using $CDCl_3$ and DMSO-d_6 as solvents. The molecular weight and dispersity of the synthesized polymer were obtained by size exclusion chromatography (SEC) using Agilent 1,100 pump, a refractive index detector, and PSS SDV (5 μm; 10^5, 10^3, and 10^2 Å; 8.0×300.0 mm) columns. THF was used as an eluent at a flow rate of 1 mL min^{-1}. A conventional calibration was constructed using poly(methyl methacrylate) (PMMA) standards. Attenuated total reflectance Fourier transform infrared (FTIR, Jasco FT/IR-4600) spectroscopy was performed to examine the functional groups. A background spectrum (32 scans at 4 cm^{-1} resolution) of a clean ATR crystal was collected and used as a reference. Differential scanning calorimetry (DSC, TA instruments, Discovery DSC 25) was performed by heating the sample to 200 °C, then cooling it to 0 °C, and reheating it to 200 °C at a rate of 10 °C min^{-1} under flowing N_2. Stress-strain measurements were performed using a dynamic mechanical analyzer (DMA, TA instruments, DMA Q850) with a rectangular specimen (length×width×thickness= 7 mm×5 mm×0.2 mm). The sample was equilibrated at 25 °C under a preload of 100 mN, and the force was increased at a rate of 0.2 N min^{-1}. A 180° peeling test was performed on a universal testing machine (DR-100 Dr TECH). The coated side of the electrode was attached to 3M tape (length×width=7.6 cm×1.8 cm), while the free side was attached to a stainless-steel substrate using double-sided tape. The 3M tape was then pulled at an angle of 180° at a displacement rate of 40 mm min^{-1}. The surface and cross-sectional morphology of the electrodes were examined by scanning electron microscopy (SEM, Tescan Vega Compact). The sample was coated with an 8 nm platinum layer before the observation. The coin cells were disassembled inside a glovebox, washed with dimethyl carbonate, and dried. The electrode was immersed in liquid nitrogen for 5 min and manually fractured while frozen.

4. Electrode Fabrication and Electrochemical Characterization

Polymer binders were dissolved in respective solvents (10 wt% CA-PNB in DMSO, 10 wt% PVDF in NMP, and 5 wt% CMC in DI water) before preparing the slurry. The slurry was prepared by mixing silicon nanoparticles (SiNP) (70 wt%), super P (15 wt%), and binder (15 wt%) in a 20 mL scintillation vial equipped with two magnetic stir bars for 24 h. The resulting slurry was cast on a copper foil using a doctor blade and vacuum dried at 70 °C for 24 h. Circular discs (diameter of 12 mm) were then punched to produce the dried electrodes and assembled to CR 2032-type coin cells using Li metal as the counter electrode (diameter of 14 mm), a polyethylene membrane (diameter of 18 mm, Wellcos, Korea) as the separator, and 1.0 M solution of $LiPF_6$ in ethylene carbonate (EC), ethyl methyl carbonate (EMC), and diethyl carbonate (DEC) (v/v/v=

30/40/30) with 10% fluoroethylene carbonate (FEC) as the electrolyte inside an argon-filled glove box. For comparison, a 1.0 M solution of $LiPF_6$ in EC/DEC (v/v=50/50) was also used as the electrolyte for some coin cells. The active material loading of the electrodes was determined to be ~0.5 mg cm^{-2}.

Galvanostatic charge/discharge tests were conducted on a battery cycler (WBCS300L, WonATech) at 27 °C in a potential range of 0.01-1.5 V (vs. Li/Li^+). All coin cells were cycled at 0.5 A g^{-1}. The prepared coin cells were aged for 12 h prior to cycling to ensure adequate electrode wetting. In the rate performance test, the current density was varied (0.1-1.0 A g^{-1}) Electrochemical impedance spectroscopy (EIS, ZIVE MP1 station, WonATech) was performed at 1.5 V in a frequency range of 100 kHz to 100 mHz. A ZMAN v2.4 EIS simulator (WonATech) integrated with a ZIVE MP1 was used to regress the impedance parameters. Cyclic voltammetry (CV) was performed on a ZIVE MP1 station with a voltage range of 0.01-3.0 V (vs. Li/Li^+) at a scan rate of 0.2 mV S^{-1}.

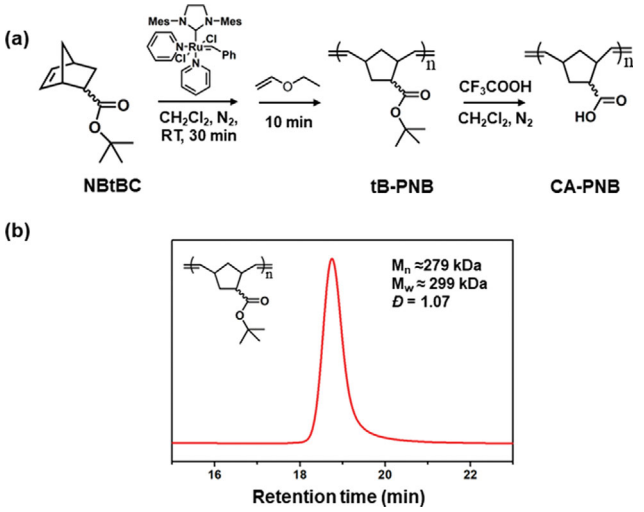

Fig. 1. (a) Synthetic route for preparing the CA-PNB binder. (b) SEC trace of t-butyl group-functionalized polynorbornene in THF.

RESULTS AND DISCUSSION

1. Synthesis and Characterization of CA-PNB Binder

The CA-PNB binder was synthesized in two steps, as shown in Fig. 1(a). The NB*t*BC monomer first underwent ROMP using a G3 catalyst at room temperature. The resulting polymer was then treated with TFA to cleave the t-butyl group, generating a carboxylic acid group. Interestingly, polymerization in the first step was completed within 30 min because of the ultrafast kinetics of ROMP when using a G3 catalyst [44]. Molecular weight characterization was performed with t-butyl group-functionalized polynorbornene to avoid clogging issues in the SEC column. The molecular weight of the polynorbornene after the first step was 279 kDa with a dispersity of 1.07 (Fig. 1(b)). The ability to obtain a high molecular weight and narrowly dispersed polymers in a fast manner under mild conditions originated from the unique characteristic of ROMP and has great benefit for saving polymerization time compared to other polymerization techniques (e.g., condensation, free-radical, emulsion, ionic, and controlled radical polymerization), which typically requires at least several hours to reach a molecular weight of tens of thousands [45-47]. In addition, since ROMP is one of the living polymerization techniques, well-defined polymers with complex architectures and controlled monomer sequences can be prepared, which may offer a powerful tool for the rational design of binders for battery electrodes.

The ^{1}H NMR and FT-IR spectra (Fig. 2(a) and 2(b)) of the monomer and the polymers were recorded to follow the polymerization and the deprotection reaction. In the ^{1}H NMR spectra, the complete disappearance of the olefinic protons of the norbornene

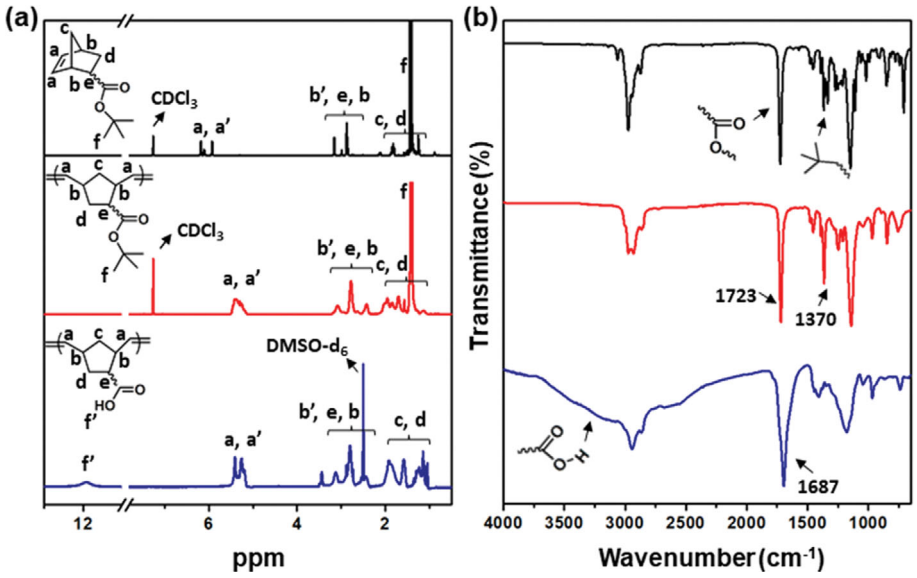

Fig. 2. (a) ^{1}H NMR and (b) FT-IR spectra: NB*t*BC monomer (top), t-butyl ester-functionalized polynorbornene (before TFA treatment, middle), and carboxylic acid-functionalized polynorbornene (after TFA treatment, bottom).

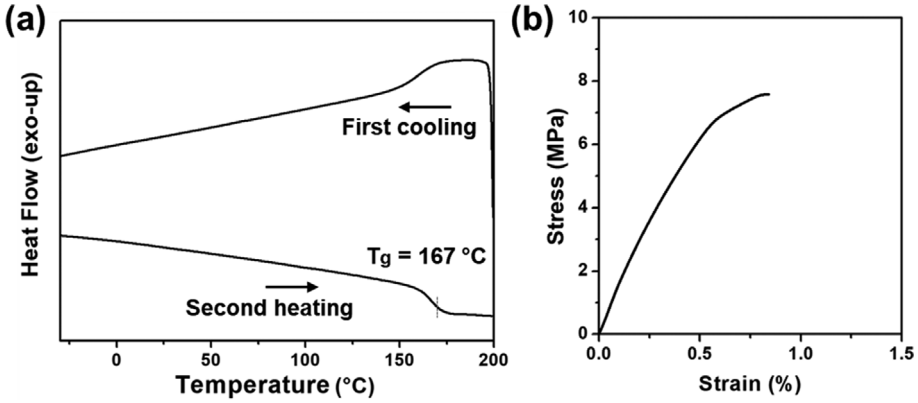

Fig. 3. (a) DSC traces of the CA-PNB during first cooling and second heating. (b) Stress-strain curves of the CA-PNB.

monomer (**a** and **a′**; 5.9-6.2 ppm) and the appearance of a new peak at 5.1-5.6 ppm corresponding to the olefinic protons of the polynorbornene indicated the completion of ROMP of NBtBC [48]. After the TFA treatment, the t-butyl group (**f**, 1.54 ppm) disappeared, and the carboxylic acid peak (**f′**, 12 ppm) appeared, both of which verified the quantitative conversion of t-butyl groups to carboxylic acids.

Deprotection of the t-butyl group was further confirmed by FT-IR spectroscopy. After the TFA treatment, a broad peak corresponding to the carboxylic acid appeared at 2,400-3,500 cm^{-1}, while the C-C vibration peak due to the t-butyl groups (1,370 cm^{-1}) disappeared [49]. In addition, the carbonyl stretching peak (C=O) shifted from 1,723 to 1,687 cm^{-1} after the TFA treatment due to the hydrogen bonding of multiple carboxylic acids. Thus, ^{1}H NMR and FT-IR analyses confirmed the synthesis of CA-PNB through the two-step reactions.

The thermal and mechanical properties of CA-PNB were characterized by DSC and DMA, as shown in Fig. 3(a) and 3(b), respectively. The glass transition temperature (T_g) of CA-PNB determined by the second heating scan was 167 °C. Such high T_g is associated with numerous intra- and intermolecular hydrogen bonding among CA-PNB chains. Note that the T_g of CA-PNB is higher than that of poly(acrylic acid), typically 105-125 °C [50], because of the more rigid backbone of polynorbornene originating from unsaturated bonds and the bridged bicyclic structure. The tensile stress-strain curve also suggests the rigid and brittle nature of the CA-PNB, exhibiting low failure strain (0.8%) and a high Young's modulus (1,638 MPa).

2. Electrochemical Properties

The electrochemical properties of the Si anode using the CA-PNB binder were evaluated in a set of half-cell tests. Fig. 4(a) presents the first two CV curves of the Si-CA-PNB anode within a voltage range between 0.01 and 3.0 V. In the initial scan, two cathodic peaks were observed at 0.86 and 0.31 V, which were ascribed to the interfacial reaction due to electrolyte reduction. These peaks were insignificant or absent in the subsequent cycle, indicating the formation of a stable SEI layer in the first cycle. The two anodic peaks at 0.36 and 0.54 V correspond to the different delithiation states of Si [51]. Fig. 4(b) shows the initial charge-discharge profiles of Si anodes prepared with different binders. In all Si anodes, a steep decline in the discharge curves was observed between 0.8 and 0.1 V, indicating the SEI formation [52,53], while the subsequent plateau at 0.1 V was associated with the formation of amorphous Li_xSi [54]. These observations were consistent with the results of the first CV scan.

Fig. 4(c) shows the specific capacity and the CE of Si anodes prepared with different binders at 0.5 A g^{-1}. The specific capacity and initial coulombic efficiency (ICE) were higher for the Si anode with the CA-PNB binder, suggesting that the CA-PNB binder effectively accommodated the volume changes of the Si anode compared with other binders. The initial discharge capacity and ICE were 3,423 mAh g^{-1} and 81% for the Si-CA-PNB electrode, 1,712 mAh g^{-1} and 74% for the Si-CMC electrode, and 1,434 mAh g^{-1} and 35% for the Si-PVDF electrode, respectively. After 100 cycles, the Si-CA-PNB anode exhibited a reversible capacity of 1,654 mAh g^{-1} with a capacity retention of 65.3% (from the 5th to 100th cycle). Although the Si-CMC anode exhibited more stable cycling behavior, the capacity was much lower than that of the Si-CA-PNB anode. The lower capacity of Si-CMC anode may be due to the less stable SEI layer on the Si surface caused by the random distribution of -COOH (or -COO^- Na^+) functional groups along the CMC backbone [55]. On the other hand, the capacity of the Si-PVDF anode decreased rapidly to 266 mAh g^{-1} at the 10th cycle. The poor cycling performance of the Si-PVDF anode was attributed to the weak interaction between the PVDF binder and the Si surface. The rate capability of the Si-CA-PNB anode was investigated further by varying the current density from 0.1-1.0 A g^{-1} (Fig. 4(d)). After 20 cycles at various current densities, the discharge capacity of the Si-CA-PNB anode recovered to 71.3% of its initial value, revealing good reversibility of the anode. Noteworthy that the FEC additive in the electrolyte substantially enhanced the electrochemical performance of the Si anode. The initial voltage profiles of the Si-CA-PNB anodes prepared with or without the FEC additive (Fig. 4(e)) showed that the ICE was 15% higher for Si-CA-PNB in the FEC-containing electrolyte (i.e., ICE of 81%) than that of the non-FEC electrolyte (i.e., ICE of 66%). Moreover, the Si-CA-PNB anode cycled in the FEC-containing electrolyte improved the cycling stability compared to that of the non-FEC electrolyte system (Fig. 4(f)). Such enhancement in the FEC system is associated with the formation of a more stable SEI layer constructed in

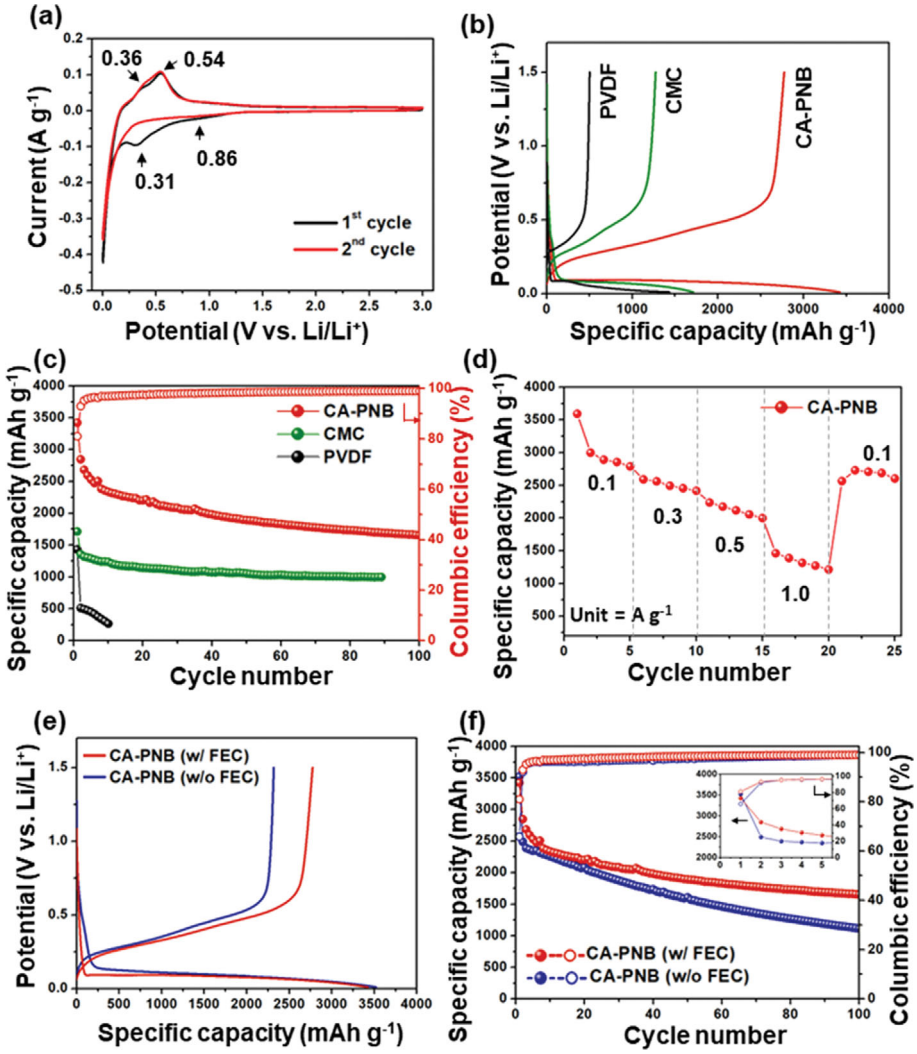

Fig. 4. (a) CV curves of Si anode prepared with CA-PNB binder. (b) Initial voltage profile of Si anodes prepared with CA-PNB, CMC, and PVDF binders at 0.5 A g^{-1}. (c) Comparison of the cycling performance of Si-anodes prepared with CA-PNB, CMC, and PVDF binders at 0.5 A g^{-1}. (d) Rate capability of the Si anode prepared with CA-PNB binder at different current densities. (e) Initial voltage profile and (f) cycling performance of Si-anodes prepared with CA-PNB binder using the electrolyte with and without FEC additive at 0.5 A g^{-1}.

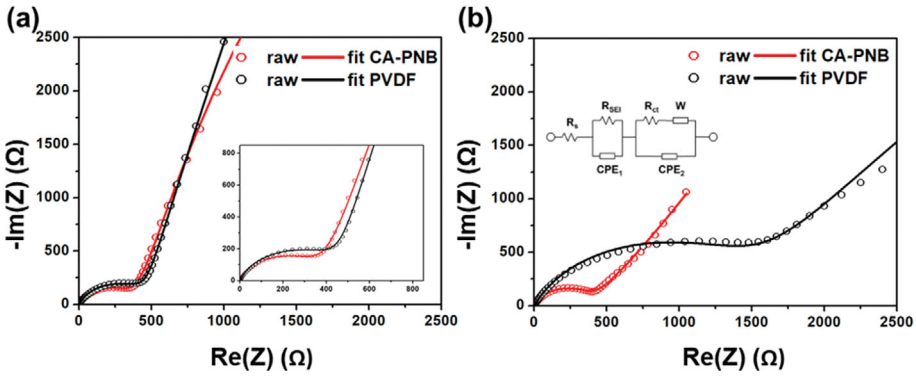

Fig. 5. Nyquist plots of the Si-CA-PNB and Si-PVDF electrodes: (a) pristine and (b) after three cycles.

the first cycle, which contains FEC decomposition products, particularly LiF [56,57]. The LiF-rich SEI layer prevents further electrolyte decomposition and reduces the irreversible capacity loss.

EIS characterization was performed to obtain more insight into

Table 1. EIS data of the Si-CA-PNB and Si-PVDF electrodes

	Pristine			After three cycles		
	R_s [Ω][a]	R_{SEI} [Ω][a]	R_{ct} [Ω][a]	R_s [Ω]	R_{SEI} [Ω]	R_{ct} [Ω]
Si-CA-PNB	1.51	460		1.67	100	520
Si-PVDF	2.23	640		2.11	934	5,400

[a]R_s, R_{SEI}, and R_{ct} are the solution, SEI, and charge-transfer resistances, respectively.

the SEI formation in Si anodes using CA-PNB and PVDF binders [58]. Fig. 5 presents Nyquist plots of the fresh and activated Si-CA-PNB anode and Si-PVDF anode, together with the equivalent circuit diagram, and Table 1 lists the regression results. In the EIS plots, the semicircle ranging from the high-mid frequency represents the SEI and charge transfer resistances (R_{SEI} and R_{ct}, respectively). The oblique line at the low-frequency region is related to the Warburg element (Z_w), which is controlled by Li^+ ion diffusion at the interface [59]. In the pristine state, the sum of R_{SEI} and R_{ct} of the Si-CA-PNB anode and Si-PVDF anode was 460 Ω and 640 Ω, respectively. After three charge-discharge cycles, the interfacial resistance of the Si-PVDF anode increased significantly, while the Si-CA-PNB anode exhibited a marginal increase in resistance (from 460 to 620 Ω), suggesting the formation of a more stable SEI layer in Si-CA-PNB anode. The formation of a stable SEI layer was attributed to the stronger interaction between the Si nanoparticles and the CA-PNB binder.

3. Adhesion and Morphological Characterization

The superior electrochemical performance of the Si anode prepared with CA-PNB compared to the control binder was elucidated further by examining the adhesion strength of the electrode using a 180° peel test. Although a thin layer of active material was peeled off from the electrode surface, the Si-CA-PNB anode exhibited an average peel strength of 1.15 N cm^{-1}, which was ~4.5 times higher than that of the Si-PVDF anode (Fig. 6(a)). Fig. 6(b) shows photographs of the electrodes after the peeling test. The copper substrate is visible in multiple sites of the Si-PVDF anode, implying that a substantial amount of active materials were detached from the surface of the Si-PVDF anode. The superior adhesion strength of the Si-CA-PNB anode originates from numerous carboxylic acid groups in the CA-PNB binder with a sufficiently high molecular weight that can have strong interactions with the silanol groups on the surface of the SiNPs. In contrast, the weak van der Waals interactions between the PVDF binder and SiNPs were inadequate for preventing the loss of active materials when subjected to peeling.

The morphology of the Si anodes before and after electrochemical cycling was examined by SEM. As shown in Fig. 7(a) and 7(b), the active materials and conductive carbon were uniformly coated on the current collector before cycling. After ten cycles, multiple microcracks appeared on the Si-CA-PNB anode, which was inevitable due to volume expansion (Fig. 7(c)). In contrast, seriously large cracks were formed on the surface of Si-PVDF anode, which also confirmed the inadequate binding force of the PVDF binder (Fig. 7(d)). Comparison of crack size between Si-CA-PNB and Si-PVDF anodes (Fig. 7(e) and 7(f)) revealed that the cracks on Si-PVDF anode are about three times larger than those on the surface of Si-CA-PNB anode. Such larger cracks can obstruct the conduction of electrons within the electrode microstructure. Fig. 7(g) and 7(h) show the photographs of the Si-CA-PNB and Si-PVDF anodes after ten cycles. While Si-CA-PNB preserved integrity despite the appearance of microcracks on the anode surface, the Si-PVDF electrode exhibited obvious disintegration and partial removal of coating layer. Both the adhesion strength and morphological analyses of the Si anodes clearly explain the disparate cycling behavior of the Si-CA-PNB and Si-PVDF anodes.

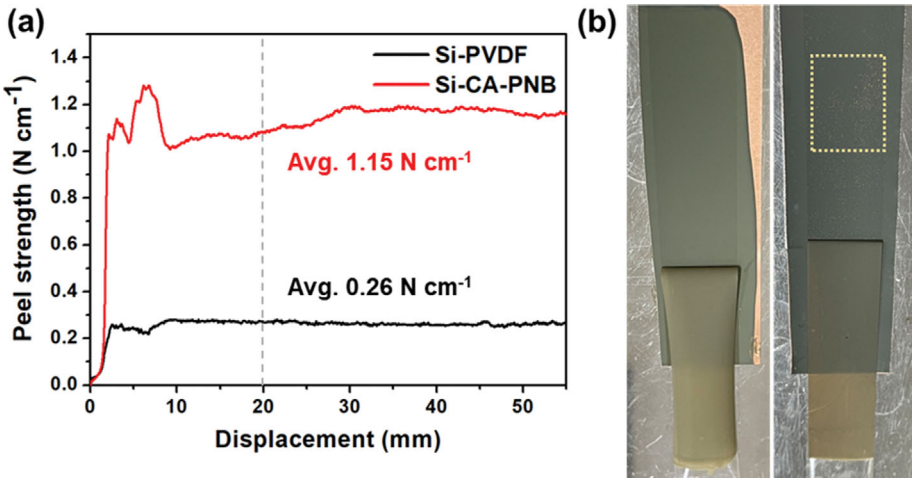

Fig. 6. (a) 180° peel test of Si-CA-PNB and Si-PVDF electrodes. (b) Photographs of Si-CA-PNB (left) and Si-PVDF (right) electrodes after the peel test. Copper foil is visible in the Si-PVDF electrode, highlighted with a yellow box.

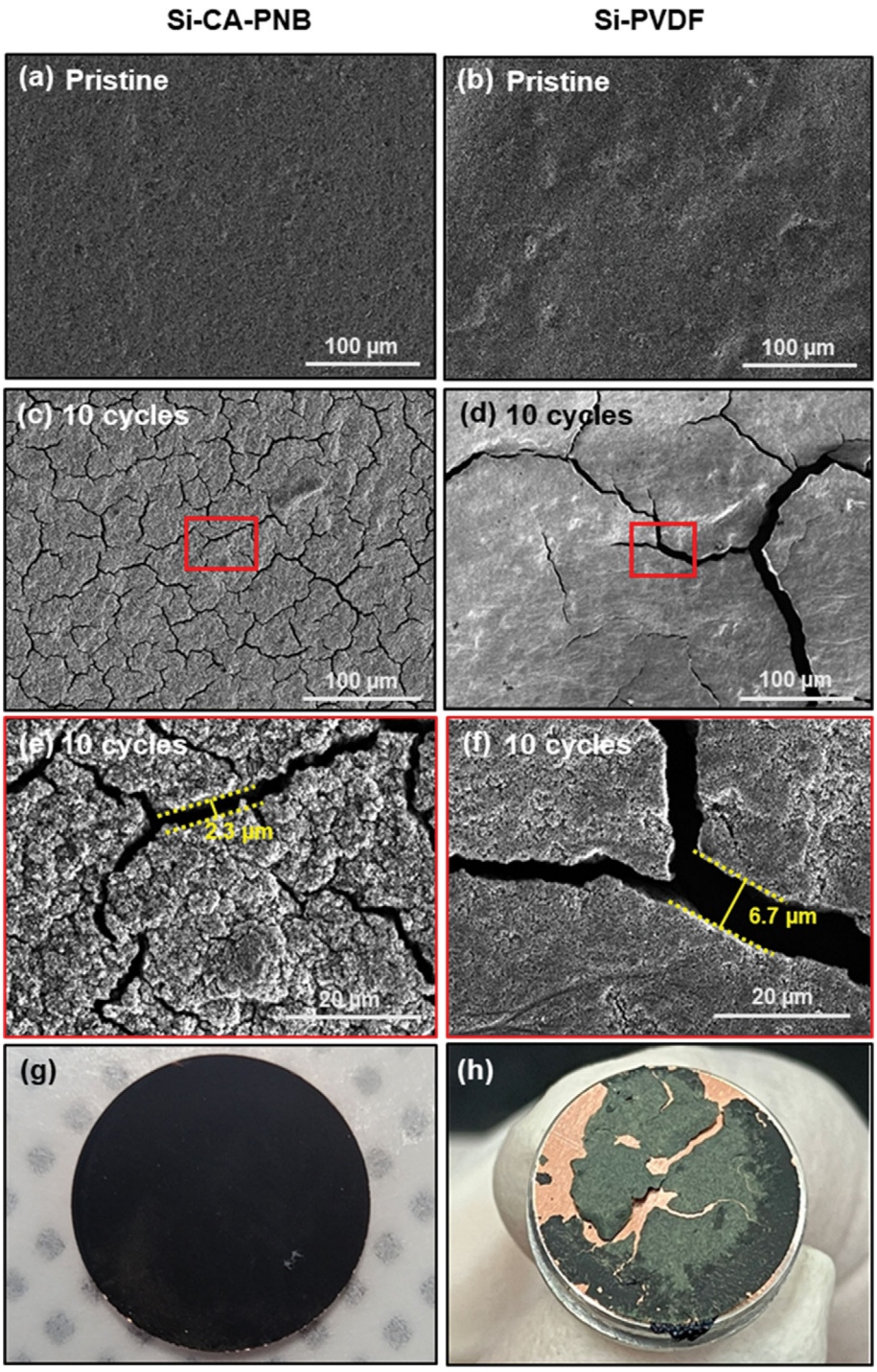

Fig. 7. Morphology of the Si-CA-PNB (left column) and Si-PVDF (right column) electrodes: ((a) and (b)) surface morphology before cycling, (c)-(f) surface morphology after ten cycles. ((g) and (h)) Photographs of the Si-CA-PNB and Si-PVDF electrode after ten cycles.

CONCLUSION

We synthesized high molecular weight carboxylic acid-functionalized polynorbornene (CA-PNB) via ROMP and investigated its potential as the binder for a Si anode. Compared to other polymerization techniques, ROMP allows the preparation of high molecular weight polymers in a fast and controlled manner without requiring harsh reaction environments. The Si anode prepared using the CA-PNB binder displayed good electrochemical performance, including an ICE of 81% and a specific capacity of 1,654 mAh g^{-1} after 100 cycles at 0.5 A g^{-1} with 65.3% capacity retention. These values are superior to the Si anodes prepared using conventional PVDF and CMC binders. The greater electrochemical performance of the CA-PNB binder is attributed to the stronger interac-

tion with the Si surface originating from the abundant carboxylic acid groups. ROMP is convenient and extremely useful for producing well-defined polymers with tailored architectures and controlled monomer sequences. Therefore, it is envisioned that ROMP is a potential tool for creating rationally designed binders for high-performance Si anodes. More efforts are currently underway and will be reported in the future.

ACKNOWLEDGEMENTS

This research was supported by the 2021 BK21 FOUR Program of Pusan National University. This work was also supported by the Basic Science Research Capacity Enhancement Project through a Korea Basic Science Institute (National Research Facilities and Equipment Center) grant funded by the Ministry of Education (2019R1 A6C1010016). The authors thank Prof. Songkil Kim for assisting with the SEM measurements with the support of the PNU Hybrid Innovative Manufacturing Engineering Center.

REFERENCES

1. F. Ozanam and M. Rosso, *Mater. Sci. Eng. B*, **213**, 2 (2016).
2. Y. Jin, B. Zhu, Z. Lu, N. Liu and J. Zhu, *Adv. Energy Mater.*, **7**, 1700715 (2017).
3. A. Du, H. Li, X. Chen, Y. Han, Z. Zhu and C. Chu, *ChemistrySelect*, **7**, e202201269 (2022).
4. M. Ashuri, Q. He and L. L. Shaw, *Nanoscale*, **8**, 74 (2016).
5. Y. An, H. Fei, G. Zeng, L. Ci, S. Xiong, J. Feng and Y. Qian, *ACS Nano*, **12**, 4993 (2018).
6. D. Vrankovic, M. Graczyk-Zajac, C. Kalcher, J. Rohrer, M. Becker, C. Stabler, G. Trykowski, K. Albe and R. Riedel, *ACS Nano*, **11**, 11409 (2017).
7. Z. Liu, X. Chang, T. Wang, W. Li, H. Ju, X. Zheng, X. Wu, C. Wang, J. Zheng and X. Li, *ACS Nano*, **11**, 6065 (2017).
8. M.-H. Park, M. G. Kim, J. Joo, K. Kim, J. Kim, S. Ahn, Y. Cui and J. Cho, *Nano Lett.*, **9**, 3844 (2009).
9. Z. Gu, C. Liu, R. Fan, Z. Zhou, Y. Chen, Y. He, X. Xia, Z. Wang and H. Liu, *Int. J. Hydrog. Energy*, **43**, 20843 (2018).
10. Y. Xu, Y. Zhu, F. Han, C. Luo and C. Wang, *Adv. Energy Mater.*, **5**, 1400753 (2015).
11. Z. Luo, Q. Xiao, G. Lei, Z. Li and C. Tang, *Carbon*, **98**, 373 (2016).
12. H. Lee, A. N. Preman, T. N. Vo, J.-H. Lee, I. T. Kim and S.-k. Ahn, *Int. J. Energy Res.*, **46**, 12565 (2022).
13. Y. Lai, H. Li, Q. Yang, H. Li, Y. Liu, Y. Song, Y. Zhong, B. Zhong, Z. Wu and X. Guo, *Ind. Eng. Chem. Res.*, **61**, 6246 (2022).
14. P. Parikh, M. Sina, A. Banerjee, X. Wang, M. S. D'Souza, J.-M. Doux, E. A. Wu, O. Y. Trieu, Y. Gong, Q. Zhou, K. Snyder and Y. S. Meng, *Chem. Mater.*, **31**, 2535 (2019).
15. A. N. Preman, H. Lee, J. Yoo, I. T. Kim, T. Saito and S.-k. Ahn, *J. Mater. Chem. A*, **8**, 25548 (2020).
16. C. Luo, L. Du, W. Wu, H. Xu, G. Zhang, S. Li, C. Wang, Z. Lu and Y. Deng, *ACS Sustain. Chem. Eng.*, **6**, 12621 (2018).
17. K. Lee, S. Lim and T.-H. Kim, *Bull. Korean Chem. Soc.*, **39**, 873 (2018).
18. D. Lee, H. Park, A. Goliaszewski, Y.-k. Byeun, T. Song and U. Paik, *Ind. Eng. Chem. Res.*, **58**, 8123 (2019).
19. M.-H. Ryou, J. Kim, I. Lee, S. Kim, Y. K. Jeong, S. Hong, J. H. Ryu, T.-S. Kim, J.-K. Park, H. Lee and J. W. Choi, *Adv. Mater.*, **25**, 1571 (2013).
20. A. Magasinski, B. Zdyrko, I. Kovalenko, B. Hertzberg, R. Burtovyy, C. F. Huebner, T. F. Fuller, I. Luzinov and G. Yushin, *ACS Appl. Mater. Interfaces*, **2**, 3004 (2010).
21. G. Zhang, Y. Yang, Y. Chen, J. Huang, T. Zhang, H. Zeng, C. Wang, G. Liu and Y. Deng, *Small*, **14**, 1801189 (2018).
22. Z. J. Han, N. Yabuuchi, S. Hashimoto, T. Sasaki and S. Komaba, *ECS Electrochem. Lett.*, **2**, A17 (2012).
23. M. T. Jeena, J.-I. Lee, S. H. Kim, C. Kim, J.-Y. Kim, S. Park and J.-H. Ryu, *ACS Appl. Mater. Interfaces*, **6**, 18001 (2014).
24. Z. Liu, S. Han, C. Xu, Y. Luo, N. Peng, C. Qin, M. Zhou, W. Wang, L. Chen and S. Okada, *RSC Adv.*, **6**, 68371 (2016).
25. Z. Cao, X. Zheng, W. Huang, Y. Wang, Q. Qu and H. Zheng, *J. Power Sources*, **463**, 228208 (2020).
26. H. Woo, K. Park, J. Kim, A. J. Yun, S. Nam and B. Park, *Adv. Mater. Interfaces*, **7**, 1901475 (2020).
27. J.-K. Yoo, J. Jeon, K. Kang and Y. S. Jung, *Electron. Mater. Lett.*, **13**, 136 (2017).
28. X. Zhu, F. Zhang, L. Zhang, L. Zhang, Y. Song, T. Jiang, S. Sayed, C. Lu, X. Wang, J. Sun and Z. Liu, *Adv. Funct. Mater.*, **28**, 1705015 (2018).
29. L. Yue, L. Zhang and H. Zhong, *J. Power Sources*, **247**, 327 (2014).
30. P.-F. Cao, G. Yang, B. Li, Y. Zhang, S. Zhao, S. Zhang, A. Erwin, Z. Zhang, A. P. Sokolov, J. Nanda and T. Saito, *ACS Energy Lett.*, **4**, 1171 (2019).
31. Z. Zheng, H. Gao, C. Ke, M. Li, Y. Cheng, D.-L. Peng, Q. Zhang and M.-S. Wang, *ACS Appl. Mater. Interfaces*, **13**, 53818 (2021).
32. Y. Gu, S. Yang, G. Zhu, Y. Yuan, Q. Qu, Y. Wang and H. Zheng, *Electrochim. Acta*, **269**, 405 (2018).
33. M. Ling, Y. Xu, H. Zhao, X. Gu, J. Qiu, S. Li, M. Wu, X. Song, C. Yan, G. Liu and S. Zhang, *Nano Energy*, **12**, 178 (2015).
34. J. Son, T. N. Vo, S. Cho, A. N. Preman, I. T. Kim and S.-k. Ahn, *J. Power Sources*, **458**, 228054 (2020).
35. P.-F. Cao, M. Naguib, Z. Du, E. Stacy, B. Li, T. Hong, K. Xing, D. N. Voylov, J. Li, D. L. Wood, III, A. P. Sokolov, J. Nanda and T. Saito, *ACS Appl. Mater. Interfaces*, **10**, 3470 (2018).
36. J.-I. Lee, H. Kang, K. H. Park, M. Shin, D. Hong, H. J. Cho, N.-R. Kang, J. Lee, S. M. Lee, J.-Y. Kim, C. K. Kim, H. Park, N.-S. Choi, S. Park and C. Yang, *Small*, **12**, 3119 (2016).
37. S. Jiang, B. Hu, Z. Shi, W. Chen, Z. Zhang and L. Zhang, *Adv. Funct. Mater.*, **30**, 1908558 (2019).
38. S. Cho, J. Son, I. Kim, H. Ahn, H.-S. Jang, S. H. Joo, K. H. Park, E. Lee, Y. Kim and S.-k. Ahn, *Polymer*, **175**, 49 (2019).
39. L. Barner, T. P. Davis, M. H. Stenzel and C. Barner-Kowollik, *Macromol. Rapid Commun.*, **28**, 539 (2007).
40. N. Hadjichristidis, H. Iatrou, M. Pitsikalis and J. Mays, *Prog. Polym. Sci.*, **31**, 1068 (2006).
41. X. Guo, B. Choi, A. Feng and S. H. Thang, *Macromol. Rapid Commun.*, **39**, 1800479 (2018).
42. H. Wang, B. Wu, X. Wu, Q. Zhuang, T. Liu, Y. Pan, G. Shi, H. Yi, P. Xu, Z. Xiong, S.-L. Chou and B. Wang, *Small*, **18**, 2101680 (2022).
43. J. A. Love, J. P. Morgan, T. M. Trnka and R. H. Grubbs, *Angew. Chem. Int. Ed.*, **41**, 4035 (2002).
44. D. J. Walsh, S. H. Lau, M. G. Hyatt and D. Guironnet, *J. Am. Chem.*

Soc., **139**, 13644 (2017).
45. Y. Pan, S. Ge, Z. Rashid, S. Gao, A. Erwin, V. Tsukruk, K. D. Vogiatzis, A. P. Sokolov, H. Yang and P.-F. Cao, *ACS Appl. Energy Mater.*, **3**, 3387 (2020).
46. S. C. Thickett and R. G. Gilbert, *Polymer*, **48**, 6965 (2007).
47. A. Goto and T. Fukuda, *Prog. Polym. Sci.*, **29**, 329 (2004).
48. P. Deshmukh, H. Yoon, S. Cho, S. Y. Yoon, O. V. Zore, T. Kim, I. Chung, S.-K. Ahn and R. M. Kasi, *J. Polymer Sci. Part A: Polym. Chem.*, **55**, 3424 (2017).
49. J. Walkowiak, M. Gradzielski, S. Zauscher and M. Ballauff, *Polymers*, **13**, 122 (2021).
50. J. J. Maurer, D. J. Eustace and C. T. Ratcliffe, *Macromolecules*, **20**, 196 (1987).
51. P. Li, G. Chen, N. Zhang, R. Ma and X. Liu, *Energy Environ. Mater.*, **4**, 72 (2021).
52. A. Wang, S. Kadam, H. Li, S. Shi and Y. Qi, *npj Comput. Mater.*, **4**, 15 (2018).
53. A. L. Michan, M. Leskes and C. P. Grey, *Chem. Mater.*, **28**, 385 (2016).
54. X. Shan, Z. Cao, G. Zhu, Y. Wang, Q. Qu, G. Liu and H. Zheng, *J. Mater. Chem. A*, **7**, 26029 (2019).
55. I. Kovalenko, B. Zdyrko, A. Magasinski, B. Hertzberg, Z. Milicev, R. Burtovyy, I. Luzinov and G. Yushin, *Science*, **334**, 75 (2011).
56. C. Xu, F. Lindgren, B. Philippe, M. Gorgoi, F. Björefors, K. Edström and T. Gustafsson, *Chem. Mater.*, **27**, 2591 (2015).
57. T. Hou, G. Yang, N. N. Rajput, J. Self, S.-W. Park, J. Nanda and K. A. Persson, *Nano Energy*, **64**, 103881 (2019).
58. X. Li, H. Chen, M. Chen, J. Qi, S. Chen and H. Zhuo, *ACS Appl. Energy Mater.*, **4**, 12709 (2021).
59. Z. H. Xie, M. Z. Rong and M. Q. Zhang, *ACS Appl. Mater. Interfaces*, **13**, 28737 (2021).